Journal of Materials Chemistry A

ROYAL SOCIETY OF CHEMISTRY

COMMUNICATION

View Article Online
View Journal | View Issue



Cite this: J. Mater. Chem. A, 2022, 10, 6470

Received 23rd January 2022
Accepted 18th February 2022

DOI: 10.1039/d2ta00623e

rsc.li/materials-a

# Nickel nanoparticles wrapped in N-doped carbon nanostructures for efficient electrochemical reduction of NO to $NH_3$†

Tamilselvan Muthusamy, Sridhar Sethuram Markandaraj and Sangaraju Shanmugam *

Production of ammonia ($NH_3$) from flue gas (*i.e.*, NO) *via* the electrocatalytic route has been considered a promising approach for rejuvenating the environment over the conventional methods. MOF-derived zero-valent nickel nanoparticles wrapped with nitrogen-doped carbon nanostructures (NiNC) were successfully grown on a carbon fiber (CF). The NiNC@CF catalyst delivered an $NH_3$ yield rate of 94 μmol $h^{-1}$ $cm^{-2}$ with significantly high faradaic efficiency (87%) at −0.5 V *vs.* RHE. Coupling with an OER catalyst in a full cell system produces 88 μmol $h^{-1}$ $cm^{-2}$ of $NH_3$ with long-term stability.

Ammonia ($NH_3$) is a building block and vital chemical in modern chemical industries such as fertilizer, pharma, and textile.[1–3] Due to the versatile application of $NH_3$, it has been produced more than 150 Mt worldwide by different strategies.[4] The mak-old Haber Bosch process is the most successful method to produce $NH_3$ on a large scale.[5] However, this $NH_3$ production method involves high temperature and pressure and the emission of greenhouse gases. Recently, the electrochemical synthesis of $NH_3$ from $H_2$ and abundant natural $N_2$ in solid oxide fuel cells and electro reduction of $N_2$ in an aqueous electrolyte is gaining tremendous attention because of their zero-emission of carbonaceous gases.[6,7] However, improper solubility of $N_2$ in the electrolyte, higher activation energy barrier, and competitive HER in the aqueous electrolytes are still formidable challenges in the large-scale production of $NH_3$.[8] Other than abundant $N_2$, few nitrogen-based oxides such as $NO_2$, $N_2O$, and NO can be used as a source of $NH_3$ production *via* the electrochemical reduction method.[9] NO is one of the major by-products of the high-temperature combustion engines and coal cracking process.[10] Since the lower concentration in the atmosphere, NO is not considered hazardous to health. However, if NO concentration increases in the atmosphere, it will lead to environmental deterioration.[11] Compared with $N_2$, NO molecules display lower bonding energy and relatively high solubility in aqueous electrolytes.[12–14] Due to this, valuable products such as $N_2H_4$, $NH_2OH$, $NH_3$ and harmless $N_2$ can be directly synthesized from NO gas *via* the electrochemical NO reduction reaction (NORR) method.[15] In addition, this process assists in restoring the pristine nature of the environment.

Few transition metals, noble metals, single-atom catalysts, and metal sulfides have been explored as electrocatalysts in the field of NORR.[16–24] Among the transition metals, Fe, Ag, and Cu nanoparticles and foils have shown promising results in the electrochemical synthesis of $NH_3$ from NO in an aqueous electrolyte.[19,21,25] However, due to NO molecule corrosive nature, the electrocatalyst, particularly metal nanoparticles, undergo degradation and dissolution in the electrolyte during the NORR process, limiting the efficiency of electrocatalyst during the long term NORR process.[25] Various strategies have been explored to enhance the chemical stability of the electrocatalyst and increase $NH_3$ yield. For example, using highly diluted NO gas enhances the yield of $NH_3$ drastically, but still, it displays poor long-term stability.[25] In some cases, introducing metal complexing agents in electrolysis improves the solubility of NO in the electrolyte, thus enhancing the electron transport and slowing down the dissolution of catalysts.[19,20,26,27] However, using metal complexes in electrolysis will interfere with the determination of $NH_3$ yield by a feasible colorimetric method. To overcome the above issues, chemically stable metal/metal composite electrocatalysts that can withstand a NO saturated aqueous electrolyte are necessary.

In this study, we explored the NC-wrapped zero-valent nickel nanoparticles on the carbon fiber (CF) and used it as a stable and efficient electrocatalyst for the NORR process. NiNC@CF possesses a strong interaction between the CF and active catalyst and chemical stability in the NO saturated electrolyte. It attains a maximal faradaic efficiency of 87% with an $NH_3$ yield rate of 94 μmol $h^{-1}$ $cm^{-2}$ under the 100% NO gas saturated electrolyte. A single cell set-up was demonstrated by coupling NORR and the anodic OER. The cell shows an $NH_3$ yield rate of 27 μmol $h^{-1}$ $cm^{-2}$ with 80% faradaic efficiency. Thus, it displays

*Department of Energy Science & Engineering, Daegu Gyeongbuk Institute of Science & Technology (DGIST), Daegu 42988, Republic of Korea. E-mail: sangarajus@dgist.ac.kr*

† Electronic supplementary information (ESI) available: Fig. S1–S18 and Tables S1, S2. See DOI: 10.1039/d2ta00623e

a high performance with long-term stability in the NORR process.

A binder-free NiNC@CF electrode was synthesized by a two-step process (Fig. 1a), as described in ESI.† In Fig. 1b, the XRD peaks appeared at 44.8, 52.1, and 76.5° corresponding to the crystallographic planes of (111), (002), and (022) of metallic Ni (PDF no. 98-005-2231). In the case of NiNC (powder), a peak at 26° was observed, which confirms the formation of low crystalline carbonous nanostructures along with metallic Ni. The FT-IR spectra show no prominent peaks in the NiNC catalyst compared to Ni-MOF (Fig. S1†). These results indicated the complete decomposition of organic functional groups in Ni-MOF frame structures and the conversion into carbonous microstructures during the pyrolysis process.

Ni-MOF@CF possesses ordered high dense nanoflakes in nature, as shown in FESEM (Fig. S2†). However, the FESEM images of NiNC@CF presented in Fig. 1c and d confirm that the initial morphology of Ni-MOF@CF nearly collapsed after thermal pyrolysis. The Ni nanoparticles were still well dispersed over porous N-doped carbon microstructures with a uniform coating on the CF surface. The elemental composition and mappings of NiNC@CF are shown in Fig. 1e. The elemental mapping results ensure the uniform dispersion of Ni, C, and N throughout the surface of CF, indicating a high distribution of NiNC nanoparticles. The HRTEM image of NiNC@CF (Fig. 1f and S3†) further confirms the even dispersion of Ni nanoparticles with an average size of 37 nm. Each of the nanoparticles has well-defined surface facets and is encapsulated with layers of carbon structures.

In addition, it is well connected by ultrathin graphene layers shown in Fig. 1f. The interlayer distance of 0.203 nm obtained from the HRTEM image represents the lattice fringe plan of (111) from Ni nanoparticles (Fig. 1g). The distance between each layer in the carbon structure is around 0.33 nm (Fig. 1h), which confirms the graphitic nature of carbon. The HAADF-STEM and elemental mapping of NiNC@CF conform to the Ni nanoparticle wrapped with N-doped carbon nanostructures (Fig. S4†). The ratio between the Ni, C, and N atoms is 72 : 27 : 1, as evaluated by C, H, N, and S elemental analysis.

The nature and degree of graphitization of the N-doped carbon microstructure in the NiNC catalyst were studied by Raman spectroscopy. In Fig. 2a, the characteristic $sp^2$ hybridization peaks appeared at 1330 and 1590 $cm^{-1}$, corresponding to the D and G bands. The intensity ratio between D and G bands ($I_D/I_G$) is around 0.85, indicating a high degree of graphitization in N-doped carbon nanostructures. In addition, a broad peak appeared at 2671 $cm^{-1}$, suggesting the presence of a few layers of graphene in NiNC@CF. It was further confirmed by the HRTEM results.

The oxidation states and survey XPS spectra reveal the presence of Ni, C, N, along with surface absorbed O atoms in NiNC@CF (Fig. S5†). High-resolution XPS spectra (Fig. 2b) of Ni 2p in NiNC@CF show high-intensity peaks at 852.9 and 870.6 eV, representing the spin–orbit doublet ($2p_{3/2}$ and $2p_{1/2}$) of zero-valent Ni atoms. This finding confirms the existence of metallic Ni from Ni-MOF. In addition, low-intensity peaks at 854.5 and 873.1 eV are also observed, and it is assigned to $Ni^{2+}$ ions from Ni–N co-ordination and surface oxidized Ni atoms. There are two satellite peaks of Ni atom also observed at the

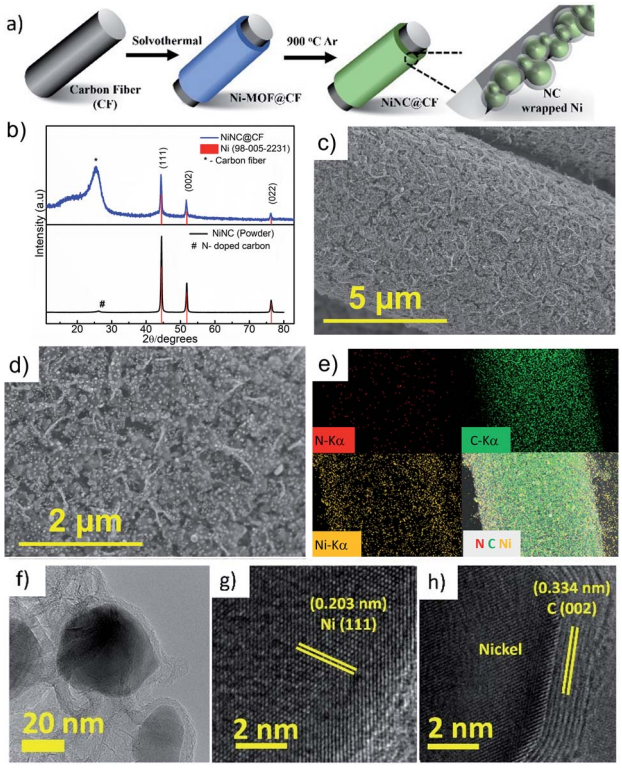


Fig. 1 (a) Schematic of the synthesis of NiNC@CF electrocatalyst. (b) XRD pattern of NiNC@CF and NiNC (powder) along with reference pattern, (c) low and (d) high magnification FESEM images of NiNC@CF, (e) FESEM elemental mapping for NiNC@CF, (f)–(h) TEM and HRTEM of NiNC@CF. The lines in (g) and (h) represent the Ni and hexagonal C lattice fringes.

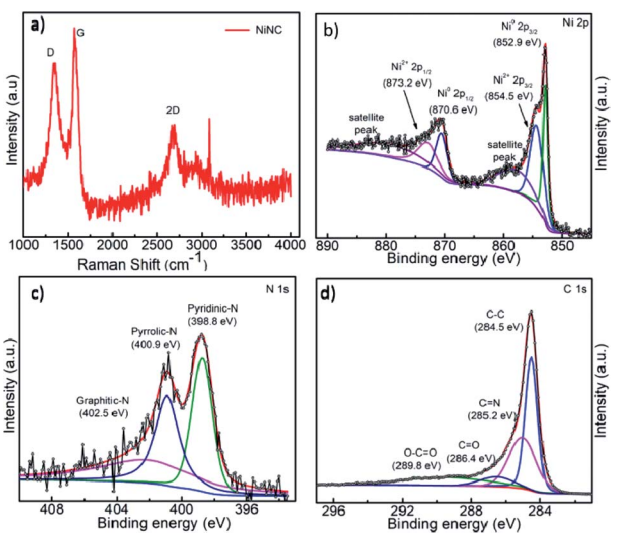


Fig. 2 (a) Raman spectra of NiNC (powder). High resolution XPS spectra of (b) Ni 2p, (c) N 1s, and (d) C 1s.

binding energies of 861 and 879 eV. By deconvoluting the core level N 1s (Fig. 2c) spectra, three peaks were obtained at 398.8, 400.9, and 402.5 eV, corresponding to the pyridinic, pyrrolic, and graphitic nature of N atoms, respectively. The high-resolution C 1s can be fitted into four characteristic peaks of carbon from various co-ordination carbon species, such as C–C (284.5 eV), C=N (285.5 eV), C=O (286.4 eV), and O–C=O (289.8 eV) (Fig. 2d).

Using the NiNC@CF catalyst as a cathode, the electrochemical synthesis of $NH_3$ from the dissolved NO gas (100%) was carried out in the PBS electrolyte (pH = 7). Fig. 3a demonstrates the LSV curves of NiNC@CF and bare CF cathode in NO and Ar saturated electrolytes. In the case of the NO saturated electrolyte, NiNC@CF shows a significant current response starting from 0.1 V *vs.* RHE, suggesting the reduction of NO gas in the electrolyte. At the higher negative potentials, the current density increases drastically, which is contributed to the high degree of NORR activity and competitive HER process. In contrast, the bare CF (current collector) shows poor electrocatalytic activity towards the NO reduction process (Fig. 3a).

The chronoamperometry (CA) curves of each electrocatalyst under various polarization potentials are acquired and plotted in Fig. S6.† At the end of a 1 h NO reduction test, the electrolyte aliquots were used to detect and quantify $NH_3$ by the standard indophenol method (see details in ESI†). The absorbance peak at 655 nm in UV visible spectra confirms the formation of $NH_3$.[28] From the results (Fig. S7†), NiNC@CF delivered the highest yield rate of $NH_3$ at −0.9 V *vs.* RHE with a faradaic efficiency of 53% (Fig. 3b). However, it displays maximum FE at −0.5 V *vs.* RHE with a relatively lower $NH_3$ yield rate (94 μmol $cm^{-2}$ $h^{-1}$).

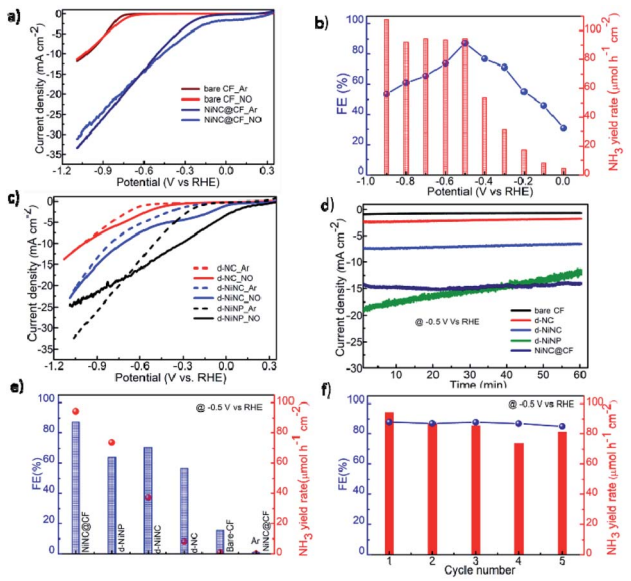


Fig. 3 (a) LSV curves of NiNC@CF and bare CF in Ar and NO saturated 0.5 M PBS. (b) $NH_3$ yield and FE of NiNC@CF in the 0.0 to −0.9 V *vs.* RHE after 1 h of NORR. (c) LSV curves of various electrodes in Ar- and NO saturated 0.5 M PBS electrolyte. (d) CA of various electrodes for NORR at −0.5 V *vs.* RHE. (e) Comparison of FE and $NH_3$ yields on various electrodes after 1 h of NORR (f) long term stability of NiNC@CF electrode at −0.5 V s. RHE.

In addition, a lower polarization potential (more positive *vs.* RHE) will be favorable to forming $N_2O$ gas products from NO gas. Moreover, the HER reaction becomes more prominent at the higher polarization potential (more negative *vs.* RHE).[29] The formation of $NH_3$ is further confirmed and quantified *via* $^1H$ NMR spectroscopy. The triplet peak in the NMR spectra (Fig. S8†) confirms the presence of $NH_3$ in the electrolyte.[30] The FE and yield values obtained from the NMR calibration curves nearly match the value calculated by the UV-visible spectroscopy technique (*vs.* ESI†). The electrolyte was further examined to detect other NO reduced products such as $NH_2OH$ and $N_2H_4$ by the NORR process. In the UV-visible spectra (Fig. S9†), the absence of the absorbance peak at $NH_2OH$ (455 nm) and $N_2H_4$ (705 nm) ruled out the formation of $NH_2OH$ and $N_2H_4$, respectively.[31,32] In Ar-saturated electrolyte (without NO), a negligible amount of $NH_3$ was detected at −0.5 V *vs.* RHE (Fig. 3c). This observation ensures that dissolved NO gas in the electrolyte is the only source for the formation of $NH_3$ during NORR. From the above finding, it can be concluded that the NC-wrapped NiNC@CF electrocatalyst delivered a superior $NH_3$ yield rate in an aqueous medium compared to reports in NRR and NORR processes (Table S2†).

The NiNC@CF electrode consists of various components such as Ni nanoparticles (NiNPs), N-doped carbon nanostructures (NC), and carbon fibre (CF). To understand the origin of the catalytic activity, each component was obtained, and their corresponding electrodes were fabricated using the drop-cast method (named as d-NiNP and d-NC, see details in ESI†). For better comparison, the NiNC (d-NiNC) electrode was also fabricated by the drop-cast method. The catalytic activity of controlled electrodes was tested using the LSV and CV. Based on the LSV (Fig. 3c), the current response in the NORR activity increases in the order: d-NC < d-NiNC < d-NiNP. From CA experiments (Fig. 3d and e), the d-NiNP electrode delivered a higher rate of ammonia yield than that of the d-NC electrode. The faradaic efficiencies were relatively comparable in both d-NiNP and d-NC electrodes. However, d-NiNP displays poor electrochemical stability, which might be due to the corrosion of NiNP from the electrode into the electrolyte during NORR (Fig. 3e). In the case of d-NiNC, the ammonia yield rate and FE is higher than d-NC and it delivered stable electrochemical performance than d-NiNP. The controlled experiments concluded that Ni nanoparticles mainly act as active sites for NO to $NH_3$ reaction and the porous N-doped carbon microstructures hinder the degradation and dissolution of Ni nanoparticles into the electrolyte. In addition, unique core–shell-like arrangements in the NiNC catalyst display synergism between the metallic Ni and N-doped nanostructures, enhancing electrocatalytic activity and chemical stability. Among all the electrodes, NiNC@CF displays relatively excellent NORR activity, which is attributed to the better electron transport between the catalyst and CF support and chemical stability.

The long-time stability of NiNC@CF was demonstrated by subjecting the electrocatalyst to five consecutive cycles (Fig. S10†). The faradaic efficiency of each cycle is maintained nearly the same (Fig. 3f). However, there is a slight loss in the rate of $NH_3$ yield. Thus, it might be attributed to the aggregation

 

and slight detachment of the catalyst from the CF surface during repeated NORR and the cleaning process after each cycle. After NORR performance, the crystallinity, morphology, and chemical stability of NiNC@CF were analyzed by the XRD, SEM, and XPS techniques. In Fig. S11,† the characteristic peaks at 44.8, 52.1, and 76.5° in the XRD pattern confirm the retention of the metallic Ni state. In the case of morphology, a slight agglomeration in the electrocatalyst surface was observed in Fig. S12.† However, the elements of the NiNC@CF catalyst were still uniformly distributed on the CF even after extended NORR performances. From the core level XPS spectra (Fig. S13†), no significant changes in composition and chemical states are observed in NiNC@CF except in N 1s XPS spectra. After deconvoluting the N 1s XPS peak, one extra peak was observed at 399.9 eV, and it was assigned to the pyrrolic-N atom. The evaluation of the new peak of the pyrrolic-N atom is attributed to the reduction of the negative charge nitrogen atom in the NiNC@CF catalyst or interaction of some pyrrolic-N with NO molecule during the NORR process.[33,34] The findings from the post electrocatalytic analysis indicate that NC layers on the Ni nanoparticles hinder the corrosion and enhance the chemical stability of NiNC@CF during the NORR process.

A prototype two-electrode (NORR/OER) electrolyzer was constructed in the H-cell by coupling commercial $RuO_2$ as an anode and NiNC@CF as a cathode. The typical non-iR compensated LSV curves are shown in Fig. 4a. The onset potential for $NH_3$ and $O_2$ formation was observed at 1.2 V. To evaluate the performance of the full cell, a series of CA were executed at a particular potential interval (Fig. 4b). From the UV-visible spectra (Fig. S14†), the potential dependent FE and $NH_3$ yield rates were calculated. Fig. 4c shows that a noticeable $NH_3$ starts producing at 1.75 V and the $NH_3$ yield rate and FE increase linearly along with applied potential. At 2.75 V, it delivered 27 μmol $cm^{-2}$ $h^{-1}$ of $NH_3$ with the highest FE (80%). Beyond 2.75 V, there is a significant loss in FE and yield rate, and it is attributed to the competitive HER process. The durability test of the NiNC@CF cathode in the full cell electrolyzer was performed by the CA over an extended period at 2.75 V. The results in Fig. 4d showed a stable current density throughout electrolysis. It disturbed the nearly identical FE and yield rate of $NH_3$.

In summary, NiNC@CF was employed as a highly durable and efficient electrocatalyst for the efficient NORR process. It delivered a high performance of reducing NO to $NH_3$ (94 μmol $h^{-1}$ $cm^{-2}$) with 87% faradaic efficiency at −0.5 V *vs.* RHE. In addition, NiNC@CF, applied as an OER catalyst in a full cell system, exhibits 27 μg $h^{-1}$ $cm^{-2}$ $NH_3$ yield with a FE of 84% and appreciable long-term stability. This electrochemical study on Ni wrapped in carbon microstructures unveils the stable catalytic activity during NORR and paves a new way to explore metal–carbon microstructures for NORR electrolyzers.

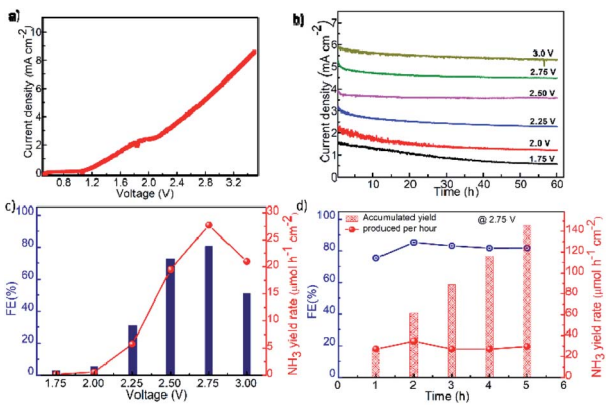


Fig. 4 (a) A single cell polarization curve in NO saturated 0.5 M PBS. (b) Chronoamperometry and (c) their corresponding FE and $NH_3$ yields at the various potential for 1 h of electrolysis. (d) Durability test of the NiNC@CF in the full cell system.

## Conflicts of interest

There are no conflicts to declare.

## Acknowledgements

This research was supported by the Mid-Level Research Program through the National Research Foundation of Korea (NRF) grant funded by the Ministry of Education (No. 2021R1A2C2009223). The authors acknowledge the Brain Korea 21 Program (BK-21) through the National Research Foundation of Korea funded by the Ministry of Education, for financially supported.

## References

1 R. Schlögl, *Angew. Chem., Int. Ed.*, 2003, **42**, 2004–2008.
2 N. Gruber and J. N. Galloway, *Nature*, 2008, **451**, 293–296.
3 H. Ray, F. Perreault and T. Boyer, *Environmental Science: Water Research & Technology*, 2022.
4 D. Bernhardt and J. Reilly, *US Geol. Surv.*, 2019, **2019**, 200.
5 H. Liu, *Ammonia synthesis catalysts: innovation and practice*, World Scientific, 2013.
6 F. Ishak, I. Dincer and C. Zamfirescu, *J. Power Sources*, 2012, **212**, 73–85.
7 D. Chanda, R. Xing, T. Xu, Q. Liu, Y. Luo, S. Liue, R. A. Tufa, T. H. Dolla, T. Montini and X. Sun, *Chem. Commun.*, 2021, **57**, 7335–7349.
8 C. J. Van der Ham, M. T. Koper and D. G. Hetterscheid, *Chem. Soc. Rev.*, 2014, **43**, 5183–5191.
9 T. Mou, J. Long, T. Frauenheim and J. Xiao, *ChemPlusChem*, 2021, **86**, 1211–1224.
10 M. Shelef, *Catal. Rev.: Sci. Eng.*, 1975, **11**, 1–40.
11 T. Boningari and P. G. Smirniotis, *Curr. Opin. Chem. Eng.*, 2016, **13**, 133–141.
12 Z. W. Seh, J. Kibsgaard, C. F. Dickens, I. Chorkendorff, J. K. Nørskov and T. F. Jaramillo, *Science*, 2017, **355**, 146.
13 H. Hirakawa, M. Hashimoto, Y. Shiraishi and T. Hirai, *ACS Catal.*, 2017, **7**, 3713–3720.
14 H. O. N. Tugaoen, S. Garcia-Segura, K. Hristovski and P. Westerhoff, *Sci. Total Environ.*, 2017, **599**, 1524–1551.
15 H. Wan, A. Bagger and J. Rossmeisl, *Angew. Chem.*, 2021, **133**, 22137–22143.

16 J. A. Colucci, M. J. Foral and S. H. Langer, *Electrochim. Acta*, 1985, **30**, 1675–1685.
17 D. H. Kim, S. Ringe, H. Kim, S. Kim, B. Kim, G. Bae, H.-S. Oh, F. Jaouen, W. Kim and H. Kim, *Nat. Commun.*, 2021, **12**, 1–11.
18 X. Peng, Y. Mi, H. Bao, Y. Liu, D. Qi, Y. Qiu, L. Zhuo, S. Zhao, J. Sun and X. Tang, *Nano Energy*, 2020, **78**, 105321.
19 D. Kim, D. Shin, J. Heo, H. Lim, J.-A. Lim, H. M. Jeong, B.-S. Kim, I. Heo, I. Oh and B. Lee, *ACS Energy Lett.*, 2020, **5**, 3647–3656.
20 L. Zhang, J. Liang, Y. Wang, T. Mou, Y. Lin, L. Yue, T. Li, Q. Liu, Y. Luo and N. Li, *Angew. Chem.*, 2021, **133**, 25467–25472.
21 J. Long, S. Chen, Y. Zhang, C. Guo, X. Fu, D. Deng and J. Xiao, *Angew. Chem.*, 2020, **132**, 9798–9805.
22 Z. Li, Z. Ma, J. Liang, Y. Ren, T. Li, S. Xu, Q. Liu, N. Li, B. Tang and Y. Liu, *Mater. Today Phys.*, 2022, **22**, 100586.
23 T. Mou, J. Liang, Z. Ma, L. Zhang, Y. Lin, T. Li, Q. Liu, Y. Luo, Y. Liu and S. Gao, *J. Mater. Chem. A*, 2021, **9**, 24268–24275.
24 J. Shi, C. Wang, R. Yang, F. Chen, N. Meng, Y. Yu and B. Zhang, *Sci. China: Chem.*, 2021, **64**, 1493–1497.
25 S. Cheon, W. J. Kim, D. Kim, Y. Kwon and J.-I. Han, Available at SSRN 3900207.
26 K. Ogura and H. Ishikawa, *J. Chem. Soc., Faraday Trans. 1*, 1984, **80**, 2243–2253.
27 E. K. Pham and S.-G. Chang, *Nature*, 1994, **369**, 139–141.
28 Y. Zhao, F. Wu, Y. Miao, C. Zhou, N. Xu, R. Shi, L. Z. Wu, J. Tang and T. Zhang, *Angew. Chem.*, 2021, **133**, 21896–21899.
29 J. Long, C. Guo, X. Fu, H. Jing, G. Qin, H. Li and J. Xiao, *J. Phys. Chem. Lett.*, 2021, **12**, 6988–6995.
30 Y. Zhao, R. Shi, X. Bian, C. Zhou, Y. Zhao, S. Zhang, F. Wu, G. I. Waterhouse, L. Z. Wu and C. H. Tung, *Adv. Sci.*, 2019, **6**, 1802109.
31 D. Frear and R. Burrell, *Anal. Chem.*, 1955, **27**, 1664–1665.
32 P. Chen, N. Zhang, S. Wang, T. Zhou, Y. Tong, C. Ao, W. Yan, L. Zhang, W. Chu and C. Wu, *Proc. Natl. Acad. Sci. U. S. A.*, 2019, **116**, 6635–6640.
33 Y. Yang, Z. Lun, G. Xia, F. Zheng, M. He and Q. Chen, *Energy Environ. Sci.*, 2015, **8**, 3563–3571.
34 B. Liu, B. He, H. Q. Peng, Y. F. Zhao, J. Y. Cheng, J. Xia, J. H. Shen, T. W. Ng, X. M. Meng, C. S. Lee and W. J. Zhang, *Adv. Sci.*, 2018, **5**, 1800406.